Continuous-time quantum Monte Carlo for fermion-boson lattice models: Improved bosonic estimators and application to the Holstein model

Manuel Weber, Fakher F. Assaad, and Martin Hohenadler
Institut für Theoretische Physik und Astrophysik, Universität Würzburg, 97074 Würzburg, Germany
(Received 8 September 2016; published 27 December 2016)

We extend the continuous-time interaction-expansion quantum Monte Carlo method with respect to measuring observables for fermion-boson lattice models. Using generating functionals, we express expectation values involving boson operators, which are not directly accessible because simulations are done in terms of a purely fermionic action, as integrals over fermionic correlation functions. We also demonstrate that certain observables can be inferred directly from the vertex distribution, and present efficient estimators for the total energy and the phonon propagator of the Holstein model. Furthermore, we generalize the covariance estimator of the fidelity susceptibility, an unbiased diagnostic for phase transitions, to the case of retarded interactions. The new estimators are applied to half-filled spinless and spinful Holstein models in one dimension. The observed renormalization of the phonon mode across the Peierls transition in the spinless model suggests a soft-mode transition in the adiabatic regime. The critical point is associated with a minimum in the phonon kinetic energy and a maximum in the fidelity susceptibility.

DOI: 10.1103/PhysRevB.94.245138

I. INTRODUCTION

Quantum Monte Carlo (QMC) methods are among the most established and powerful tools to solve the quantum many-body problem of correlated electrons. In particular, the auxiliary-field QMC method [1] and the stochastic series expansion (SSE) representation [2] are widely used to simulate lattice models, whereas more recent continuous-time (CTQMC) methods [3,4] are predominantly applied as impurity solvers in dynamical mean-field theory (DMFT) [5]. Recently, progress has been made in the development of new methods to simulate fermionic lattice models [6,7], the solution of the fermionic sign problem for specific models [8–11], and the calculation of novel observables such as the entanglement entropy [12–19] and the fidelity susceptibility [20–23].

For a large class of QMC methods (e.g., SSE and CTQMC), the partition function is calculated stochastically in a series expansion and operators that are sampled can be measured directly from the Monte Carlo configurations. In this paper, we consider the continuous-time interaction expansion (CT-INT) method [3]. In CT-INT, the configurations are sets of interaction vertices and expectation values are usually calculated from the single-particle Green's function using Wick's theorem [24]. However, it can be advantageous to exploit the information contained in the distribution of vertices, an important example being the fidelity susceptibility [23].

The action-based formulation of the CT-INT method in particular allows efficient simulations of fermion-boson lattice models [25], and has been successfully applied to electron-phonon problems [26–29]. If the action is quadratic in the bosonic fields, the latter can be integrated out exactly [30], resulting in a fermionic action with retarded interactions. Remarkably, autocorrelations, which can be prohibitively strong in cases where the bosons are sampled explicitly [31], are significantly reduced in the fermionic representation.

An apparent disadvantage of the fermionic approach is the loss of access to bosonic observables. However, as shown here, the latter can be systematically calculated from fermionic correlation functions using sum rules derived from generating functionals. Information about the bosonic fields is also encoded in the distribution of vertices. For a local fermion-boson interaction (e.g., the Holstein model [32]), the bosonic contributions to the total energy as well as the local bosonic propagator can be calculated efficiently from the vertex distribution. Moreover, with the help of auxiliary Ising fields [33] originally introduced to avoid the sign problem [25], even nonlocal correlation functions such as the full bosonic propagator become accessible. Similar techniques have been applied to solve fermion-boson problems with DMFT and the hybridization expansion (CT-HYB) method [4] to understand dynamical screening effects [34–36], and in extended DMFT calculations [37,38]. The usefulness of such techniques for computationally expensive lattice problems was so far unclear but is demonstrated here. Finally, we derive an estimator for the fidelity susceptibility applicable to retarded boson-mediated interactions that can be used to identify phase transitions.

We apply these (improved) estimators to one-dimensional Holstein models [32]. These fundamental models for the effects of electron-phonon interaction constitute a significant numerical challenge due to the infinite phonon Hilbert space, and the different time scales for the fermion and boson dynamics. In the half-filled case considered here, they describe a quantum phase transition from a metallic phase to a Peierls insulator with long-range charge-density-wave order [39,40]. We investigate two important open questions, namely, the renormalization of the phonon spectrum across the Peierls transition in the adiabatic regime, and two alternative diagnostics (phonon kinetic energy, fidelity susceptibility) to locate the critical point. Importantly, our methodological developments can also be applied in higher dimensions and for other models.

The paper is organized as follows. In Sec. II, we discuss the calculation of observables from the vertex distribution in a general formulation of the CT-INT method. In Sec. III, we derive the effective fermionic action for fermion-boson models and obtain estimators for the total energy and the phonon propagator of the Holstein model. The calculation of bosonic observables from the vertex distribution with the CT-INT method is discussed in Sec. IV. A performance test and results

for Holstein models are presented in Sec. V. We conclude in Sec. VI, and provide appendixes on the relation between bosonic observables and the dynamic charge-structure factor as well as on further improvements of the estimators.

II. QUANTUM MONTE CARLO METHOD

A. General formulation of the CT-INT method

The CT-INT method [3] is based on the path-integral formulation of the grand-canonical partition function

$$Z = \int \mathcal{D}(\bar{c},c)\, e^{-S_0[\bar{c},c]-S_1[\bar{c},c]}, \tag{1}$$

where the fermions are given in the Grassmann coherent-state representation $\hat{c}\,|c\rangle = c\,|c\rangle$ and time ordering is implicit. We split the action into the free-fermion part S_0 and the interaction S_1. The weak-coupling perturbation expansion of Eq. (1) is

$$\frac{Z}{Z_0} = \sum_{n=0}^{\infty} \frac{(-1)^n}{n!} \langle S_1^n \rangle_0, \tag{2}$$

where we have defined $\langle O\rangle_0 = Z_0^{-1} \int \mathcal{D}(\bar{c},c)\, e^{-S_0} O$ with $Z_0 = \int \mathcal{D}(\bar{c},c)\, e^{-S_0}$. In the CT-INT method, the expansion in Eq. (2) is calculated stochastically by sampling configurations of interaction vertices. For this purpose, we write the interaction in the vertex notation

$$S_1 = \sum_{\nu} w_\nu h_\nu. \tag{3}$$

A vertex is represented by an instance of the superindex ν that contains both discrete (e.g., lattice sites) and continuous variables (e.g., imaginary times), a weight w_ν, and the Grassmann representation of the operators $h_\nu[\bar{c},c]$. The perturbation expansion becomes

$$\frac{Z}{Z_0} = \sum_{n=0}^{\infty} \underbrace{\sum_{\nu_1 \ldots \nu_n}}_{\sum_{C_n}} \underbrace{\frac{(-1)^n}{n!}\, w_{\nu_1} \ldots w_{\nu_n} \langle h_{\nu_1} \ldots h_{\nu_n} \rangle_0}_{W[C_n]}. \tag{4}$$

The sum runs over the expansion order n and all configurations of vertices $C_n = \{\nu_1, \ldots, \nu_n\}$ for a given n. We can identify the weight $W[C_n]$ to be sampled with the Metropolis-Hastings algorithm [41,42], which involves the determinant $\langle h_{\nu_1} \ldots h_{\nu_n} \rangle_0 = \det M[C_n]$ of the $\mathcal{O}(n) \times \mathcal{O}(n)$ matrix $M[C_n]$ whose entries are noninteracting Green's functions. Updates correspond to the addition or removal of individual vertices, and involve matrix-vector multiplications with $\mathcal{O}(n^2)$ operations. Since $\mathcal{O}(n)$ updates are necessary to reach an independent configuration, the algorithm scales as $\mathcal{O}(n^3)$. The average expansion order $\langle n\rangle$ scales linearly with the system size L and the inverse temperature $\beta = (k_B T)^{-1}$ [3] (see below). Expectation values $\langle O\rangle = Z^{-1} \int \mathcal{D}(\bar{c},c)\, e^{-S_0-S_1} O$ are calculated via

$$\langle O\rangle = \sum_{n=0}^{\infty} \sum_{C_n} p[C_n] \langle\langle O\rangle\rangle_{C_n}, \tag{5}$$

where $p[C_n] = W[C_n] / \sum_n \sum_{C_n} W[C_n]$ and $\langle\langle O\rangle\rangle_{C_n}$ is the value of the observable for configuration C_n. For any C_n, Wick's theorem [24] can be used to calculate $\langle\langle O\rangle\rangle_{C_n}$ from the single-particle Green's function. However, especially the calculation of the time-displaced Green's function can be expensive because a matrix-vector multiplication of $\mathcal{O}(n^2)$ must be performed for each imaginary time τ and each pair of lattice sites. For further details, see Ref. [5].

B. Estimators from the vertex distribution

In the SSE method [2], operators contained in the operator string are accessible from the Monte Carlo configurations, whereas in the CT-HYB method [4] the single-particle Green's function can be obtained directly from the perturbation expansion. Similarly, in CT-INT, expectation values of operators h_ν contained in the interaction S_1 can be calculated efficiently from the distribution of vertices [43]. To this end, h_ν is regarded as an additional vertex written as $h_\nu = w_\nu^{-1} \sum_{\nu_{n+1}} w_{\nu_{n+1}} h_{\nu_{n+1}} \delta_{\nu,\nu_{n+1}}$ and absorbed into the perturbation expansion:

$$\begin{aligned}
\langle h_\nu\rangle &= \frac{Z_0}{Z} \sum_{n=0}^{\infty} \sum_{C_n} \frac{(-1)^n}{n!}\, w_{\nu_1} \ldots w_{\nu_n} \langle h_{\nu_1} \ldots h_{\nu_n} h_\nu \rangle_0 \\
&= -\frac{1}{w_\nu} \sum_{n=0}^{\infty} \sum_{C_{n+1}} (n+1)\, p[C_{n+1}]\, \delta_{\nu,\nu_{n+1}} \\
&= \sum_{n=0}^{\infty} \sum_{C_n} p[C_n] \left[-\frac{1}{w_\nu} \sum_{k=1}^{n} \delta_{\nu,\nu_k} \right].
\end{aligned} \tag{6}$$

Here, we first identified the probability distribution $p[C_{n+1}]$ of a configuration with $n+1$ vertices and then shifted the summation index to obtain $p[C_n]$. Finally, we included the $n=0$ contribution to the sum and replaced the factor of n by a sum over the equivalent vertices. Comparison with Eq. (5) yields

$$\langle\langle h_\nu\rangle\rangle_{C_n} = -\frac{1}{w_\nu} \sum_{k=1}^{n} \delta_{\nu,\nu_k}. \tag{7}$$

From Eq. (7) we obtain the familiar relation between the interaction term and the average expansion order $\langle S_1\rangle = -\langle n\rangle$ [3]. Because $\langle S_1\rangle$ is an extensive thermodynamic quantity, the average expansion order $\langle n\rangle \sim \beta L$. In the same way, we can obtain higher-order correlation functions, e.g.,

$$\langle\langle h_\nu h_{\nu'}\rangle\rangle_{C_n} = \frac{1}{w_\nu w_{\nu'}} \sum_{k\neq l} \delta_{\nu,\nu_k} \delta_{\nu',\nu_l}. \tag{8}$$

Each variable contained in ν can be resolved from a configuration C_n, but continuous variables (e.g., imaginary time τ) have to be integrated over (at least on a small interval) to make sense of the corresponding delta functions. The evaluation of observables via Eqs. (7) and (8) only requires $\mathcal{O}(n)$ operations since

$$\sum_{k\neq l} f_{ik} f_{jl} = \sum_k f_{ik} \sum_l f_{jl} - \sum_k f_{ik} f_{jk}. \tag{9}$$

Because only operators that appear in the interaction can be measured, the cheaper vertex measurements cannot completely replace the more expensive calculation of the single-particle Green's function. However, the class of accessible

observables grows with the complexity of the interaction, as demonstrated below for the fermion-boson problem.

C. Fidelity susceptibility

Recently, Wang *et al.* [23] derived a universal QMC estimator for the fidelity susceptibility χ_F based on the distribution of vertices. We briefly summarize their results, focusing on the CT-INT method.

The fidelity susceptibility is a geometrical tool originating from quantum information theory [44]. It can be used to detect quantum critical points without prior knowledge of the order parameter from the change of the ground state upon changing the Hamiltonian $\hat{H}(\alpha) = \hat{H}_0 + \alpha \hat{H}_1$ via a driving parameter α. In Refs. [20–22], χ_F was generalized to finite temperatures in terms of the structure factor

$$\chi_F(\alpha) = \int_0^{\beta/2} d\tau [\langle \hat{H}_1(\tau)\hat{H}_1(0)\rangle - \langle \hat{H}_1(0)\rangle^2]\tau. \quad (10)$$

Wang *et al.* [23] recognized that Eq. (10) can be recovered from the distribution of vertices using Eqs. (7) and (8), leading to the covariance estimator

$$\chi_F = \frac{\langle n_L n_R\rangle - \langle n_L\rangle\langle n_R\rangle}{2\alpha^2}. \quad (11)$$

For each vertex configuration, n_L and n_R count the number of vertices in the intervals $[0,\beta/2)$ and $[\beta/2,\beta)$, respectively. The calculation of χ_F via Eq. (11) is restricted to fermionic actions that are local in time and related to a Hamiltonian, i.e., $S_1 = \alpha \int d\tau H_1(\tau)$. A generalization to retarded boson-mediated interactions is given below.

III. PATH-INTEGRAL FORMULATION OF THE FERMION-BOSON PROBLEM

In the following, we derive an effective fermionic action for a generic fermion-boson model that can be simulated with the CT-INT method. With the help of generating functionals, any bosonic observable can be recovered from fermionic correlation functions. In particular, we derive sum rules for the phonon propagator and the total energy of the Holstein model.

A. Fermion-boson models

We consider a generic one-dimensional fermion-boson Hamiltonian of the form

$$\hat{H} = \hat{H}_0 + \sum_q \omega_q \hat{b}_q^\dagger \hat{b}_q + \sum_q \gamma_q(\hat{\rho}_q \hat{b}_q^\dagger + \hat{\rho}_q^\dagger \hat{b}_q), \quad (12)$$

with fermionic (bosonic) creation and annihilation operators $\hat{c}^\dagger$, $\hat{c}$ ($\hat{b}^\dagger$, $\hat{b}$) and the free-fermion part $\hat{H}_0[\hat{c}^\dagger,\hat{c}]$. $\hat{H}$ is restricted to be quadratic in the bosons, but we allow a general dispersion ω_q and a coupling to an arbitrary fermionic operator $\hat{\rho}_q[\hat{c}^\dagger,\hat{c}]$ with coupling parameter γ_q.

As an example, we consider the Holstein model [32]

$$\hat{H} = \hat{H}_0 + \sum_i \left(\frac{1}{2M}\hat{P}_i^2 + \frac{K}{2}\hat{Q}_i^2\right) + g\sum_i \hat{Q}_i\hat{\rho}_i, \quad (13)$$

where the electronic part is given by the nearest-neighbor hopping of spinful fermions with amplitude t,

$$\hat{H}_0 = -t\sum_{i\sigma}(\hat{c}_{i\sigma}^\dagger \hat{c}_{i+1\sigma} + \hat{c}_{i+1\sigma}^\dagger \hat{c}_{i\sigma}). \quad (14)$$

The phonons are described by local harmonic oscillators with displacements $\hat{Q}_i$ and momenta $\hat{P}_i$; M is the oscillator mass and K the spring constant. The displacements couple to the charge density $\hat{\rho}_i = \sum_\sigma(\hat{n}_{i\sigma} - 1/2)$ (here $\hat{n}_{i\sigma} = \hat{c}_{i\sigma}^\dagger \hat{c}_{i\sigma}$) with coupling parameter g. The spinless Holstein model is obtained by dropping spin indices.

The Holstein model follows from the generic model (12) by dropping the momentum dependence of the bosons, i.e., $\omega_q \to \omega_0$ and $\gamma_q \to \gamma$, and assuming a density-displacement coupling so that $\hat{\rho}_q^\dagger = \hat{\rho}_{-q}$. The same simplifications arise in electron-phonon models with nonlocal density-displacement [27] or bond-displacement couplings [29]. Therefore, the formulas derived below for the Holstein model can be easily transferred to other models. For the Holstein case, $\omega_0 = \sqrt{K/M}$, $\gamma = g/\sqrt{2M\omega_0}$, and we also introduce the dimensionless coupling parameter $\lambda = \gamma^2/(2\omega_0 t) = g^2/(4Kt)$. Simulations were performed at half-filling, but the estimators are general.

B. Effective fermionic action for the bosons and observables from generating functionals

For the generic fermion-boson model (12), the partition function takes the form

$$Z = \int \mathcal{D}(\bar{c},c)\, e^{-S_0[\bar{c},c]} \int \mathcal{D}(\bar{b},b)\, e^{-S_{ep}[\bar{c},c,\bar{b},b]}. \quad (15)$$

We use the coherent-state representation $\hat{c}\,|c\rangle = c\,|c\rangle$ with Grassmann variables c for the fermions, and $\hat{b}\,|b\rangle = b\,|b\rangle$ with complex variables b for the bosons. The action is split into the fermionic part S_0 and the remainder S_{ep} containing the free-boson part and the interaction

$$S_{ep} = \int_0^\beta d\tau \sum_q \{\bar{b}_q(\tau)[\partial_\tau + \omega_q]b_q(\tau) + \gamma_q[\rho_q(\tau)\bar{b}_q(\tau) + \bar{\rho}_q(\tau)b_q(\tau)]\}. \quad (16)$$

The bosons can be integrated out exactly [30], leading to an effective fermionic interaction

$$S_1 = -\sum_q \frac{\gamma_q^2}{\omega_q} \iint_0^\beta d\tau\, d\tau' \bar{\rho}_q(\tau)\, P_q(\tau-\tau')\, \rho_q(\tau') \quad (17)$$

mediated by the noninteracting bosonic Green's function $P_q(\tau-\tau') = \omega_q\langle \bar{b}_q(\tau)b_q(\tau')\rangle_0$. Here, $\langle\ldots\rangle_0$ also denotes expectation values with respect to the free-boson part of the action. For $0 \leqslant \tau < \beta$, $P_q(\tau)$ is given by

$$P_q(\tau) = \omega_q \frac{e^{-\omega_q\tau}}{1-e^{-\omega_q\beta}} \quad (18)$$

and we impose $P_q(\tau+\beta) = P_q(\tau)$. With the factor of ω_q, the adiabatic and antiadiabatic limits of $P_q(\tau)$ are

$$\lim_{\omega_q\to 0} P_q(\tau) = \frac{1}{\beta}, \quad \lim_{\omega_q\to\infty} P_q(\tau) = \delta(\tau). \quad (19)$$

In principle, the fermionic interaction (17) can be simulated with the CT-INT method if transformed into real space. However, for any nontrivial dispersion ω_q the transformed bosonic propagator has negative contributions that cause a sign problem [29]. Therefore, we focus on models with optical bosons, i.e., $\omega_q = \omega_0$.

To obtain estimators for bosonic correlation functions in the CT-INT method, we add the source term

$$S_{\text{source}} = -\int_0^\beta d\tau \sum_q [\eta_q(\tau)\,\bar{b}_q(\tau) + \bar{\eta}_q(\tau)\,b_q(\tau)] \tag{20}$$

to S_{ep}. After integrating out the bosons, the complex source fields $\eta_q(\tau)$ and $\bar{\eta}_q(\tau)$ appear in S_1, i.e.,

$$S_{1,\text{source}} = -\sum_q \frac{\gamma_q^2}{\omega_q} \iint_0^\beta d\tau\, d\tau' \big[\bar{\rho}_q(\tau) - \gamma_q^{-1}\bar{\eta}_q(\tau)\big] \times P_q(\tau-\tau')\big[\rho_q(\tau') - \gamma_q^{-1}\eta_q(\tau')\big]. \tag{21}$$

From Eq. (21), any bosonic correlation function can be expressed in terms of fermionic fields by taking functional derivatives and the limit $\eta \to 0$.

C. Application to the Holstein model

In the following, we illustrate the use of this formalism for the Holstein model (13). The notation is kept as general as possible to facilitate applications to other models. Replacing $P_q(\tau) \to P(\tau)$, the effective interaction

$$S_1 = -2\lambda t \iint_0^\beta d\tau\, d\tau' \sum_i \rho_i(\tau)\, P(\tau-\tau')\, \rho_i(\tau') \tag{22}$$

becomes diagonal in real space. To express bosonic observables in terms of the displacements $q_i(\tau)$ or the momenta $p_i(\tau)$ we rewrite the source term (20) as

$$S_{\text{source}} = -\int_0^\beta d\tau \sum_i [\xi_i(\tau)\, q_i(\tau) + \zeta_i(\tau)\, p_i(\tau)], \tag{23}$$

with real fields $\xi_i(\tau)$ and $\zeta_i(\tau)$. Transformation of the source fields in Eq. (21) leads to the action

$$S_{1,\text{source}} = S_1 + S^+_{\xi\rho} + S^+_{\xi\xi} + S^-_{\zeta\rho} + S^+_{\zeta\zeta} + S^-_{\xi\zeta}, \tag{24}$$

where the individual contributions are given by

$$S^\pm_{\mu\nu} = -\alpha_{\mu\nu} \iint_0^\beta d\tau\, d\tau' \sum_i \mu_i(\tau)\, P_\pm(\tau-\tau')\, \nu_i(\tau') \tag{25}$$

with $\alpha_{\xi\rho} = -2\sqrt{\lambda t/K}$, $\alpha_{\xi\xi} = 1/(2K)$, $\alpha_{\zeta\rho} = 2i\sqrt{M\lambda t}$, $\alpha_{\zeta\zeta} = M/2$, and $\alpha_{\xi\zeta} = i/\omega_0$. Here, we defined the phonon propagators $P_\pm(\tau) = \frac{1}{2}[P(\tau) \pm P(\beta-\tau)]$, corresponding to $P_+(\tau-\tau') = K\,\langle q_i(\tau) q_i(\tau')\rangle_0 = M^{-1}\langle p_i(\tau) p_i(\tau')\rangle_0$ and $P_-(\tau-\tau') = -i\,\omega_0 \langle q_i(\tau) p_i(\tau')\rangle_0$.

With the help of the generating functionals in Eqs. (24) and (25), we get access to the phonon propagators

$$K\,\langle q_i(\tau) q_j(\tau')\rangle = P_+(\tau-\tau')\,\delta_{i,j} + X^{++}_{ij}(\tau,\tau'), \tag{26}$$

$$\frac{1}{M}\langle p_i(\tau) p_j(\tau')\rangle = P_+(\tau-\tau')\,\delta_{i,j} + X^{--}_{ij}(\tau,\tau') \tag{27}$$

consisting of the free propagator P_+ and the interaction contributions

$$X^{\pm\pm}_{ij}(\tau,\tau') = 4\lambda t \iint_0^\beta d\tau_1 d\tau_1'\, P_\pm(\tau-\tau_1) \times \langle \rho_i(\tau_1)\rho_j(\tau_1')\rangle P_\pm(\tau_1'-\tau'). \tag{28}$$

The total energy is $E = E^{\text{kin}}_{\text{e}} + E^{\text{kin}}_{\text{ph}} + E^{\text{pot}}_{\text{ph}} + E_{\text{eph}}$, with

$$E^{\text{kin}}_{\text{ph}} = \frac{E^0_{\text{ph}}}{2} - 2\lambda t \iint_0^\beta d\tau\, d\tau'\, P_-(\tau)\, P_-(\tau')\, C_\rho(\tau-\tau'), \tag{29}$$

$$E^{\text{pot}}_{\text{ph}} = \frac{E^0_{\text{ph}}}{2} + 2\lambda t \iint_0^\beta d\tau\, d\tau'\, P_+(\tau)\, P_+(\tau')\, C_\rho(\tau-\tau'), \tag{30}$$

$$E_{\text{eph}} = -4\lambda t \int_0^\beta d\tau\, P_+(\tau)\, C_\rho(\tau). \tag{31}$$

Here, $E^0_{\text{ph}} = L\,P_+(0)$ and $C_\rho(\tau-\tau') = \sum_i \langle \rho_i(\tau)\rho_i(\tau')\rangle$. $E^{\text{pot}}_{\text{ph}}$ and $E^{\text{kin}}_{\text{ph}}$ follow from Eqs. (26) and (27) by fixing the interaction to $X^{\pm\pm}_{ii}(0,0)$. In Appendix A, we provide further information on the relation between the bosonic observables and the dynamic charge structure factor.

The observables (26)–(31) can be recovered from the charge correlation function $\langle \rho_i(\tau)\rho_j(\tau')\rangle$ which is accessible in CT-INT via Wick's theorem. In Ref. [45], we calculated $\langle \rho_i(\tau)\rho_j(0)\rangle$ on an equidistant τ grid with spacing $\Delta\tau_{\text{obs}} = 0.1$ and performed the remaining integrals numerically. However, as shown below, it is more efficient to use the distribution of vertices.

IV. CT-INT FOR THE HOLSTEIN MODEL

A. Vertex notation for the effective interaction

For the Holstein model, the interaction term sampled with the CT-INT method takes the form

$$S_1 = -\lambda t \iint_0^\beta d\tau\, d\tau' \sum_{i\sigma\sigma' s} [\rho_{i\sigma}(\tau) - s\delta] \times P_+(\tau-\tau')[\rho_{i\sigma'}(\tau') - s\delta]. \tag{32}$$

Compared to Eq. (22), we introduced an auxiliary Ising variable $s = \pm 1$ (and $\delta = 0.51$) to avoid the sign problem [25], and used the symmetrized phonon propagator $P_+(\tau)$. In the notation of Eq. (3), $\nu = \{i,\tau,\tau',\sigma,\sigma',s\}$, $w_\nu = -\lambda t\, P_+(\tau-\tau')$, and

$$h_\nu = \rho_{i\sigma}(\tau)\rho_{i\sigma'}(\tau') + \delta^2 - s\delta[\rho_{i\sigma}(\tau) + \rho_{i\sigma'}(\tau')]. \tag{33}$$

The QMC simulation is performed as described before. The acceptance rate for adding a new vertex can be optimized by proposing $\tau - \tau'$ according to $P_+(\tau-\tau')$ via inverse transform sampling.

B. Observables from the distribution of vertices

The operators contained in Eq. (33) can be measured from the distribution of vertices. In particular, we have access to the dynamical charge correlations required for the calculation

of the bosonic observables in Sec. III C. In the following, we use Eqs. (7) and (8) to derive improved estimators for the total energy, the fidelity susceptibility, and the phonon propagator.

1. Total energy

The kinetic energy of the electrons is calculated from the single-particle Green's function. To recover the phononic contributions (29)–(31) from the distribution of vertices, we sum over the auxiliary Ising variable s in Eq. (33) and use Eq. (7) to obtain the estimator

$$\langle\langle \rho_{i\sigma}(\tau)\rho_{i\sigma'}(\tau')\rangle\rangle_{C_n} + \delta^2 = \sum_{k=1}^{n} \frac{\delta_{i,i_k}\delta_{\sigma,\sigma_k}\delta_{\sigma',\sigma'_k}\delta(\tau-\tau_k)\,\delta(\tau'-\tau'_k)}{2\lambda t\, P_+(\tau_k-\tau'_k)} \tag{34}$$

for the local charge-charge correlation function. From Eq. (34) we get the estimators

$$E_{\mathrm{ph}}^{\mathrm{kin}}[C_n] = \frac{E_{\mathrm{ph}}^0}{2} - \sum_{k=1}^{n} \frac{P_-(\tau_k)P_-(\tau'_k)}{P_+(\tau_k-\tau'_k)}, \tag{35}$$

$$E_{\mathrm{ph}}^{\mathrm{pot}}[C_n] = \frac{E_{\mathrm{ph}}^0}{2} + \sum_{k=1}^{n} \frac{P_+(\tau_k)P_+(\tau'_k)}{P_+(\tau_k-\tau'_k)} - 2\lambda t L N_\sigma^2\delta^2, \tag{36}$$

$$E_{\mathrm{eph}}[C_n] = -\frac{2n}{\beta} + 4\lambda t L N_\sigma^2\delta^2. \tag{37}$$

For the kinetic energy the term $\sim\delta^2$ vanishes due to the antisymmetry of $P_-(\tau)$. N_σ counts the number of spin components of the Holstein model, i.e., $N_\sigma = 1$ for the spinless and $N_\sigma = 2$ for the spinful model.

The estimators (35) and (36) can be further improved by exploiting the global translational invariance of all vertices, i.e., $\tau_k \to \tau_k + \Delta\tau$ and $\tau'_k \to \tau'_k + \Delta\tau$ with $\Delta\tau \in [0,\beta)$. We integrate over $\Delta\tau$ to treat all the translations exactly (see Appendix B for details). Thereby, especially $E_{\mathrm{ph}}^{\mathrm{kin}}[C_n]$ is substantially improved, as shown in Sec. V A.

2. Fidelity susceptibility

To calculate the fidelity susceptibility for a retarded interaction we start from Eq. (10) and identify the electron-phonon coupling as the driving term with $\alpha = g$ and $\hat{H}_1 = \sum_i \hat{Q}_i\hat{\rho}_i$. The displacements $\hat{Q}_i$ entering the expectation values of the Hamiltonian in Eq. (10) can be replaced with fermionic operators using the source terms introduced before. $\langle H_1\rangle$ is given by Eq. (31), and

$$\langle H_1(\tau)H_1(\tau')\rangle = 2\sum_{\nu_1} w_{\nu_1}\langle h_{\nu_1}\rangle\delta(\tau-\tau_1)\,\delta(\tau'-\tau'_1) + 4\sum_{\nu_1\nu_2} w_{\nu_1}w_{\nu_2}\langle h_{\nu_1}h_{\nu_2}\rangle\delta(\tau-\tau'_1)\,\delta(\tau'-\tau'_2) \tag{38}$$

in the vertex notation of the Holstein model. Continuing the derivation as in Ref. [23], we obtain an estimator very similar to Eq. (11),

$$\chi_{\mathrm{F}} = \frac{\langle\tilde{n}_{\mathrm{L}}\tilde{n}_{\mathrm{R}}\rangle - \langle\tilde{n}_{\mathrm{L}}\rangle\langle\tilde{n}_{\mathrm{R}}\rangle}{2g^2}. \tag{39}$$

However, in the present case, each vertex contains two bilinears with times τ_k and τ'_k, and $\tilde{n}_{\mathrm{L}}$ and $\tilde{n}_{\mathrm{R}}$ count the numbers of these bilinears in the left and right half of the partitioned imaginary-time axis. For simplicity, we omitted a constant shift in Eq. (39) that arises from the δ-dependent terms in Eq. (33). Taking it into account leads to $\chi_{\mathrm{F}} \to \chi_{\mathrm{F}} - 2\lambda t L N_\sigma^2\delta^2\tanh(\beta\omega_0/4)/(\omega_0 g^2)$.

3. Phonon propagator

Equation (34) only gives access to local charge-charge correlations. For the Holstein model, we can also obtain nonlocal correlation functions from the distribution of vertices, including the phonon propagator. For this purpose, we exploit the information provided by the Ising variable s. If we consider $\sum_s s\,h_\nu$, the first two terms in Eq. (33) drop out and only individual charge operators are left. Analogously, by taking

$$\sum_{s_1s_2} s_1s_2\,h_{\nu_1}h_{\nu_2} = 4\delta^2\big[\rho_{i_1\sigma_1}(\tau_1) + \rho_{i_1\sigma'_1}(\tau'_1)\big] \times\big[\rho_{i_2\sigma_2}(\tau_2) + \rho_{i_2\sigma'_2}(\tau'_2)\big], \tag{40}$$

we can recover nonlocal charge correlations from Eq. (8). The simplest estimator is the charge susceptibility

$$\chi_{ij}[C_n] = \frac{1}{\beta}\iint d\tau\,d\tau'\langle\langle\rho_i(\tau)\rho_j(\tau')\rangle\rangle_{C_n} = \frac{1}{16(\lambda t)^2N_\sigma^2\delta^2\beta^3}\sum_{k\neq l}\frac{s_k\,\delta_{i,i_k}}{P_+(\tau_k-\tau'_k)}\frac{s_l\,\delta_{j,i_l}}{P_+(\tau_l-\tau'_l)}, \tag{41}$$

which is obtained from the summation over all variables except for the lattice sites. Similarly, the (spin-resolved) charge correlation function can be calculated directly in Matsubara frequencies. The phonon propagators (26) and (27) take the form

$$K\langle\langle q_i(\tau)q_j(\tau')\rangle\rangle_{C_n} = P_+(\tau-\tau')\,\delta_{i,j} + \frac{1}{4\lambda t N_\sigma^2\delta^2}\sum_{k\neq l}\frac{P_+(\tau-\tau_k)P_+(\tau-\tau'_k)\,s_k\,\delta_{i,i_k}}{P_+(\tau_k-\tau'_k)}\frac{P_+(\tau'-\tau_l)P_+(\tau'-\tau'_l)\,s_l\,\delta_{j,i_l}}{P_+(\tau_l-\tau'_l)}, \tag{42}$$

$$\frac{1}{M}\langle\langle p_i(\tau)p_j(\tau')\rangle\rangle_{C_n} = P_+(\tau-\tau')\,\delta_{i,j} - \frac{1}{\lambda t N_\sigma^2\delta^2\beta^2}\sum_{k\neq l}\frac{P_-(\tau-\tau_k)\,s_k\,\delta_{i,i_k}}{P_+(\tau_k-\tau'_k)}\frac{P_-(\tau'-\tau_l)\,s_l\,\delta_{j,i_l}}{P_+(\tau_l-\tau'_l)}. \tag{43}$$

To arrive at Eq. (42), we multiplied Eq. (40) with the symmetrized propagator P_+ for each of the four times on the right-hand side before integrating over the imaginary times. For Eq. (43), we included the antisymmetrized propagator P_-

only for one pair of times, but the estimator can be further improved by considering the remaining three combinations. Similar to $E_{\mathrm{ph}}^{\mathrm{kin}}[C_n]$, the estimator (43) can be substantially improved by exploiting translational invariance of the vertices (see Appendix B).

V. RESULTS

A. Performance of the vertex measurements

In the CT-INT method, the computation of the single-particle Green's function for the calculation of observables via Wick's theorem requires $\mathcal{O}(n^2 L N_\tau)$ operations, where N_τ is the number of τ points. If N_τ is scaled with β, the calculation of dynamical correlation functions is of the same order as the Monte Carlo updates. For fermion-boson problems, even the bosonic energies in Eqs. (29)–(31) require the full time dependence of $\langle \rho_i(\tau)\rho_j(0)\rangle$. On the other hand, the calculation from the vertex distribution involves only $\mathcal{O}(n)$ operations for the energies and $\mathcal{O}(nN_\tau)$ for the phonon propagator. For the latter, exploiting translational invariance leads to another $\mathcal{O}(L^2 N_\tau^2)$ operation to set up the final estimator (cf. Appendix B). For large n, the computational cost for the vertex measurements becomes negligible.

The above considerations were verified for the spinless Holstein model with $\omega_0/t = 0.4$, $L = \beta t = 22$, $\lambda = 1.5$, and 1000 QMC steps between measurements. The average expansion order was $\langle n\rangle \approx 660$ and we used $\Delta\tau_{\mathrm{obs}} = 0.1$ ($N_\tau = 220$). The computation of dynamical correlation functions using Wick's theorem took 26% of the total time, of which 86% went into the matrix-vector multiplications necessary to calculate the Green's function. Only 1% of the total time was used for the vertex measurements, most of which went into the $\mathcal{O}(L^2 N_\tau^2)$ operations necessary to set up the translation-invariant phonon propagator. If we omitted this last operation, the vertex measurements only took 0.02% of the total time, and were dominated by the exact evaluation of $P_\pm(\tau)$ for each vertex. Approximately the same time would be needed for equal-time measurements from Wick's theorem using $N_\tau = 1$. Hence, further improvements through tabulation of $P_\pm(\tau)$ seem unnecessary.

Aside from the significant speedup, another advantage of the vertex measurements is the exact calculation of imaginary-time integrals. In contrast, Wick's theorem provides $\langle \rho_i(\tau)\rho_j(0)\rangle$ only on a finite grid so that systematic errors from numerical integration can arise. For $\omega_0/t = 0.4$, using Simpson's rule on an equidistant grid with $\Delta\tau_{\mathrm{obs}} = 0.1$ was sufficient to make systematic errors irrelevant. However, more elaborate integration schemes may be necessary for larger ω_0.

Table I reports ratios of statistical errors of averages obtained from either the vertex distribution or Wick's theorem, as determined in the same simulation and hence for the same number of bins. We considered different bosonic energies, as well as the charge susceptibility $\chi(q)$ at $q = \pi$ which tracks charge-density-wave order. For $E_{\mathrm{ph}}^{\mathrm{pot}}$ and $E_{\mathrm{ph}}^{\mathrm{kin}}$ we compared three different estimators: the simple estimators (35) and (36) from one set of vertices, the improved estimators using translational invariance [Eq. (B1)], and the estimators for the phonon propagators using the Ising spins, Eqs. (42) and (43).

TABLE I. Ratios of statistical errors for averages from vertex measurements and Wick's theorem for different simulation parameters. The reference point is the spinless Holstein model with $\omega_0/t = 0.4$, $\lambda = 0.5$, $L = \beta t = 22$, and $\delta = 0.51$. The first two rows indicate the observable and estimator used. The last column reports the average expansion order.

Observable	E_{eph}	$E_{\mathrm{ph}}^{\mathrm{pot}}$			$E_{\mathrm{ph}}^{\mathrm{kin}}$			$\chi(\pi)$	$\langle n\rangle$
from Eq.	(37)	(36)	(B1)	(42)	(35)	(B1)	(43)	(41)	
Reference	2.6	4.0	2.6	2.5	20	5.6	5.9	1.2	151
$\lambda = 1.0$	1.2	1.4	1.1	1.2	4.8	1.6	1.3	1.0	371
$\lambda = 1.5$	1.1	1.3	1.1	1.6	18	3.3	2.9	1.0	661
$L = \beta t = 14$	3.2	4.0	3.2	0.2	19	6.4	4.0	1.2	62
$L = \beta t = 30$	2.6	5.0	2.7	2.8	23	5.4	13	1.3	282
$\delta = 1.0$	3.7	7.0	4.0	2.1	32	8.5	4.4	1.2	510

The reference results are for the spinless Holstein model with $\omega_0/t = 0.4$, $\lambda = 0.5$, $L = \beta t = 22$, and $\delta = 0.51$. For the resulting rather small expansion order $\langle n\rangle \approx 151$, the estimators from Wick's theorem have better statistics, i.e., the ratios in Table I are larger than one. The vertex estimators improve significantly upon exploiting translational invariance, especially $E_{\mathrm{ph}}^{\mathrm{kin}}$. Increasing the number of vertices per phase-space volume via the interaction parameter λ levels out the differences between estimators, except for $E_{\mathrm{ph}}^{\mathrm{kin}}$ at $\lambda = 1.5$. In contrast, changing $\langle n\rangle$ via the phase-space parameters L and β leaves most of the ratios essentially unchanged. The same is true when increasing the number of vertices via the Ising-spin parameter δ. Finally, Table I confirms that $\langle n\rangle \sim \beta L$, whereas the dependence on λ is nonlinear.

Although the dependence of the statistical errors on the simulation parameters is not completely systematic, the vertex measurements become advantageous especially at large expansion orders. The errors are of the same order of magnitude, but the vertex estimators are much faster and avoid systematic integration errors.

B. Peierls transition in Holstein models

The Peierls quantum phase transition in half-filled spinful Holstein and Holstein-Hubbard models has been studied with a number of numerical techniques (see Ref. [46] for a review). While early QMC results [47] suggested the absence of a metallic phase, more recent work has established a phase transition at a nonzero critical value λ_c [40,48] in accordance with functional renormalization group results [49]. However, the exact determination of the phase boundary, as well as the characterization of the metallic phase in terms of Luttinger liquid parameters remain open problems [46]. The difficulties are associated with the Berezinskii-Kosterlitz-Thouless (BKT) nature of the transition, so that gaps are exponentially small near λ_c, and a small but nonzero spin gap caused by attractive backscattering which is hard to resolve numerically [46]. In particular, the spin gap renders the previously used charge susceptibility [50] essentially useless for detecting long-range charge order [46]. In contrast, no such complications are encountered for the spinless Holstein model. Although the quantum phonons still represent a significant numerical

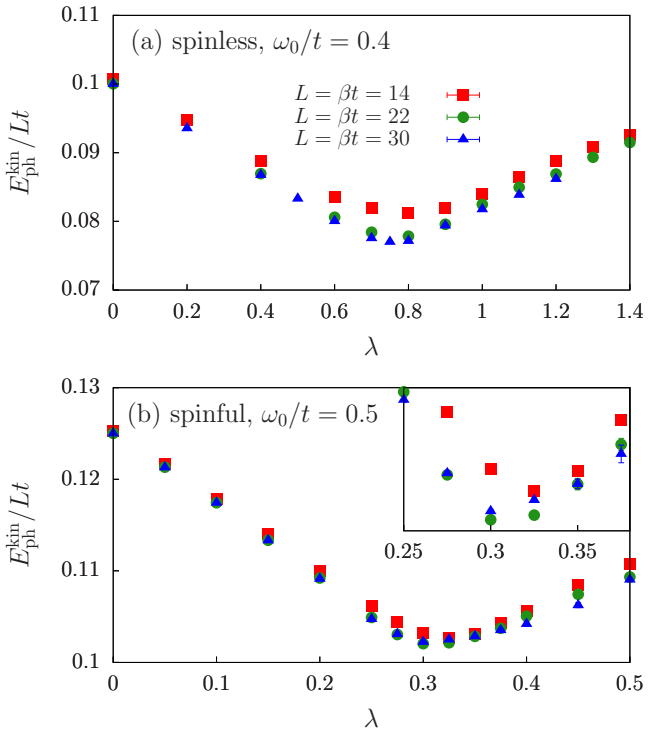

FIG. 1. Phonon kinetic energy per site for (a) the spinless Holstein model with $\omega_0/t = 0.4$ and (b) the spinful Holstein model with $\omega_0/t = 0.5$. The inset in (b) shows a closeup of the region around the minimum.

challenge, the phase diagram and the Luttinger liquid parameters have been determined quite accurately [51,52].

Here, we consider alternative diagnostics to detect the Peierls transition, namely, the phonon kinetic energy and the fidelity susceptibility. In addition, we present significantly improved results for the phonon spectral function over the entire coupling range.

1. Phonon kinetic energy

Figure 1 shows the phonon kinetic energy for the spinless Holstein model with $\omega_0/t = 0.4$ and the spinful Holstein model with $\omega_0/t = 0.5$. For both models, $E_{\rm ph}^{\rm kin}$ exhibits a distinct minimum as a function of λ. In the spinless case, $E_{\rm ph}^{\rm kin}$ has almost converged for the largest system size considered ($L = 30$) and the position of the minimum is consistent with the previous estimate $\lambda_c \approx 0.7$ [51]. While the critical value of the spinful model is still under debate [46], the position of the minimum in Fig. 1(b) suggests a slightly larger value than in previous results where $\lambda_c \approx 0.25$ [46,53]. The nonmonotonic finite-size dependence of $E_{\rm ph}^{\rm kin}(L)$ near λ_c in the spinful case is expected to arise from the small but nonzero spin gap in the metallic phase [46].

The minimum in $E_{\rm ph}^{\rm kin}$ can be related to the behavior of the dynamic charge structure factor $S_\rho(q,\omega)$ using the sum rules derived in Appendix A. Because of the density-displacement coupling, $S_\rho(q,\omega)$ also contains contributions from the renormalized phonon dispersion $\tilde{\omega}(q)$. The minimum of $E_{\rm ph}^{\rm kin}$ near λ_c arises from the softening and subsequent hardening of $\tilde{\omega}(q)$ near $q = \pi$ discussed below. Interestingly, a minimum of the phonon kinetic energy is also observed in the crossover from a large to a small polaron in the Holstein model [54,55].

The renormalization of $\tilde{\omega}(q)$ was also used in Ref. [56] to estimate λ_c from fits to the phonon Green's function. In our results (see below and Ref. [45]), the value of λ at which complete softening of the phonon mode occurs matches the position of the minimum in $E_{\rm ph}^{\rm kin}$. The latter quantity is easier and faster to calculate with the CT-INT method. For the spinless Holstein model, we have also tested this estimator for other phonon frequencies. At $\omega_0/t = 1$, the position of the minimum in $E_{\rm ph}^{\rm kin}$ approaches the critical coupling $\lambda_c \approx 1.3$ from density-matrix renormalization group calculations [52], but CT-INT simulations become difficult at these stronger couplings. At $\omega_0/t = 0.1$, we find considerable finite-size effects even at $\beta t = L = 42$ where the position of the minimum still deviates significantly from $\lambda_c \approx 0.4$ [52].

2. Phonon spectral function

Previous results for the spinless Holstein model suggest that in the adiabatic regime considered here, the phonon dispersion softens at and around $q = \pi$ (the ordering wave vector for the Peierls transition) on approaching λ_c from the metallic phase [26,45,51,56,57]. For a soft-mode transition, the phonon mode should become completely soft at $q = \pi$ and $\lambda = \lambda_c$, and subsequently harden for $\lambda > \lambda_c$. Indications for such a hardening were recently observed for the spinful Holstein model [45], but a clear identification is complicated by the dominant central peak in the Peierls phase [26,45] and, in the case of exact diagonalization, the small system sizes accessible at strong coupling [51].

Here, we consider the phonon spectral functions

$$B_\alpha(q,\omega) = \frac{1}{Z}\sum_{mn} e^{-\beta E_m} \left| \langle m | \hat{O}_q^\alpha | n \rangle \right|^2 \delta(\omega - \Delta_{nm}) \quad (44)$$

calculated either from the displacement [$\alpha = Q$, Eq. (26)] or the momentum correlation function [$\alpha = P$, Eq. (27)], with $\hat{O}^Q = K^{1/2}\hat{Q}$, $\hat{O}^P = M^{-1/2}\hat{P}$, and $\Delta_{nm} = E_n - E_m$.

In principle, both spectral functions contain the same information, but spectral weights may differ significantly. In particular, the Monte Carlo estimators (42) and (43) may be subject to different statistical fluctuations that affect the stochastic analytic continuation [58,59].

The displacement spectrum $B_Q(q,\omega)$ in Fig. 2(a) reveals the softening of the phonons near $q = \pi$ in the metallic phase. Near the critical point, the dispersion appears completely soft at $q = \pi$ [Fig. 2(b)], and the spectrum is dominated by a central peak at $\omega = 0$ associated with the long-range charge order. This peak grows strongly with λ and introduces strong fluctuations in the dynamic displacement correlation function (26) at all momenta q. The fluctuations cause a significant broadening of the spectrum obtained by analytic continuation, and in particular make it virtually impossible to resolve finite-frequency contributions at $q = \pi$ [cf. Fig. 2(c)].

To follow the phonon dispersion in the ordered phase, we instead consider the spectral function $B_P(q,\omega)$ shown in Figs. 2(d)–2(f). The use of the momentum correlation function (27) filters out the central mode, and allows us to unambiguously identify the hardening of the phonon

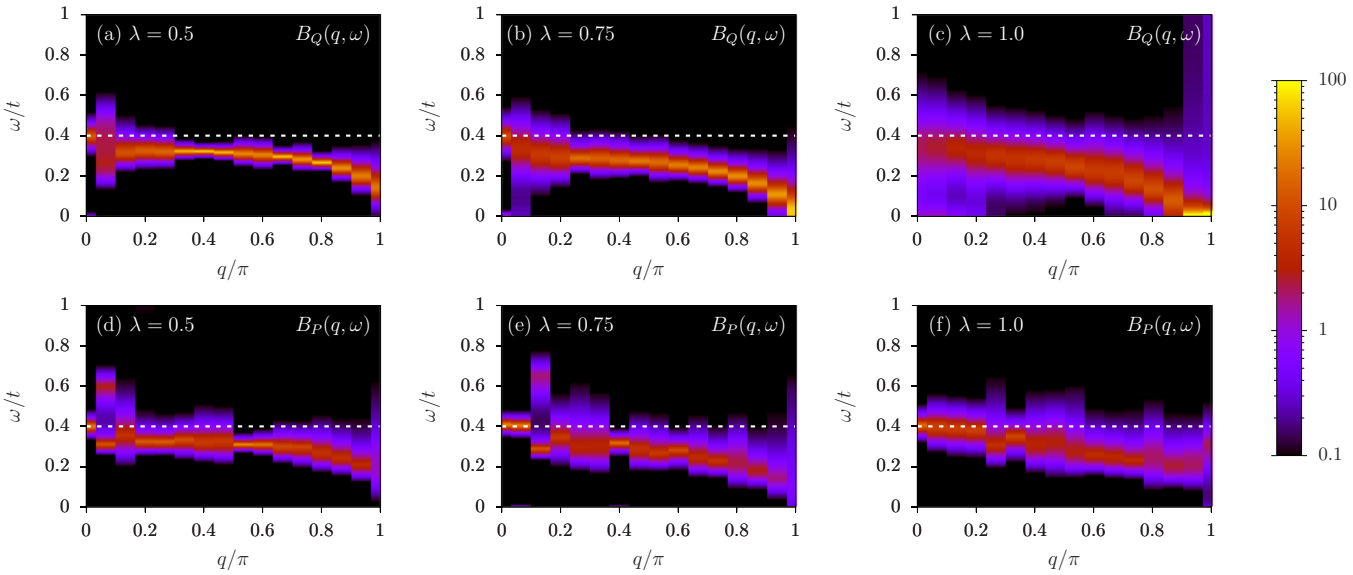

FIG. 2. Phonon spectral functions $B_Q(q,\omega)$ [(a)–(c)] and $B_P(q,\omega)$ [(d)–(f)] for the spinless Holstein model. Dashed lines correspond to $\omega_0/t = 0.4$. Here, $L = \beta t = 30$.

dispersion at $q = \pi$ in the Peierls phase [Fig. 2(f)]. Hence, the Peierls transition in the adiabatic regime can be classified as a soft-mode transition.

3. *Fidelity susceptibility*

Using the estimator (39) we calculated the fidelity susceptibility χ_F for the spinless and the spinful Holstein model. The phonon frequencies were chosen as in Fig. 1.

Figure 3(a) shows χ_F/L for the spinless Holstein model as a function of λ. We find a maximum that grows and shifts to smaller λ with increasing L. In contrast, finite-size effects are smaller at weak and strong coupling. In the thermodynamic limit, a cusp at the critical coupling is expected for a BKT transition [60]. For the accessible system sizes, the position of the maximum deviates significantly from the expected value $\lambda_c \approx 0.7$ [51], in contrast to Fig. 1(a). A slow convergence of the fidelity susceptibility with system size was previously observed for the BKT transition in the spin-$\frac{1}{2}$ XXZ chain [60].

Results for the spinful Holstein model are shown in Fig. 3(b). We again observe a maximum at intermediate values of λ that are significantly larger than previous estimates $\lambda_c \approx 0.25$ [46,53] and the position of the minimum in Fig. 1(b). Finite-size effects appear to be less systematic than for the spinless case, which we attribute to the additional spin gap; the latter is not fully resolved for small L [46]. The results in Fig. 3(b) are consistent with a phase transition at a $\lambda_c > 0$ and hence a metallic phase at weak coupling, as reported in previous work.

VI. CONCLUSIONS

The CT-INT quantum Monte Carlo method is particularly useful to simulate fermion-boson models because the bosons can be integrated out. While advantageous for simulations, this integration makes it nontrivial to calculate expectation values of bosonic variables. In this work, we presented estimators for arbitrary bosonic correlation functions using generating functionals. As a concrete example, we derived sum rules for the total energy and the phonon propagator of the Holstein model. Moreover, we showed that several observables of interest can be measured directly from the vertex distribution instead of using Wick's theorem. Additionally, we generalized the QMC estimator for the fidelity susceptibility [23] to

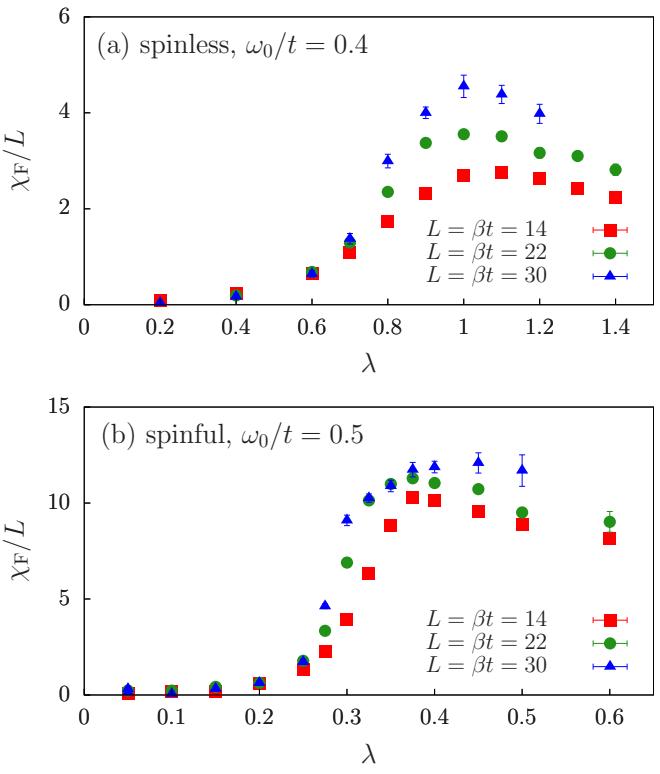

FIG. 3. Fidelity susceptibility per site for (a) the spinless Holstein model with $\omega_0/t = 0.4$ and (b) the spinful Holstein model with $\omega_0/t = 0.5$. Results were obtained from Eq. (39) with $g^2 \to \lambda = g^2/(4Kt)$ and including the shift discussed after Eq. (39).

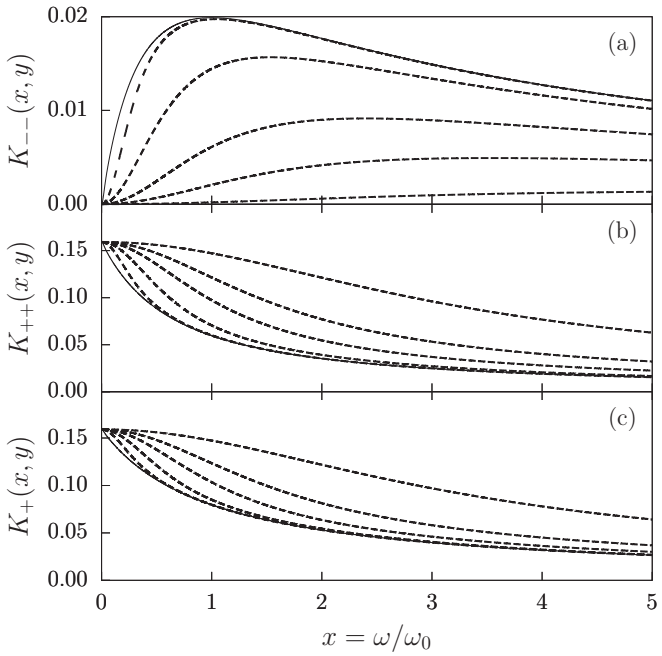

FIG. 4. The kernels K_{--}, K_{++}, and K_{+}. Solid lines correspond to $T = 0$ results, whereas dashed lines correspond to $y = \beta\omega_0 = \{10,5,3,2,1\}$ as shown from the top in (a) and from the bottom in (b) and (c).

retarded boson-mediated interactions, thereby providing a rather general diagnostic to detect phase transitions.

A comparison of different observables and simulation parameters showed that statistical errors are of the same order for the vertex estimators and the estimators based on Wick's theorem. The vertex estimators are easy to implement, more efficient, and often avoid systematic errors from numerical integration. These findings complement previous applications in the context of impurity problems. Our results are general and can be applied to a variety of other lattice fermion-boson models. For example, the possibility to calculate the total energy provides access to the specific heat. Moreover, the calculation of the charge susceptibility from the auxiliary Ising spins may be advantageous to detect charge order in higher dimensions or in Hubbard-type models.

These methodological developments were applied to one-dimensional spinless and spinful Holstein models for electron-phonon interaction. The phonon kinetic energy was found to exhibit a minimum related to the renormalization (softening) of the phonon mode. For intermediate phonon frequencies, the location of the minimum is consistent with other estimates of the critical point. The phonon spectral function calculated from the phonon momentum correlator reveals the hardening of the phonon mode in the Peierls phase, and thereby provides evidence for the soft-mode nature of the Peierls transition. Finally, the fidelity susceptibility exhibits a broad maximum at intermediate coupling and significant finite-size effects. While it hence does not provide more accurate critical values in the one-dimensional case considered, the qualitatively similar behavior observed for the spinless and the spinful model may be regarded as additional evidence for an extended metallic phase in the latter.

ACKNOWLEDGMENTS

The authors gratefully acknowledge the computing time granted by the John von Neumann Institute for Computing (NIC) and provided on the supercomputer JURECA [61] at Jülich Supercomputing Centre, as well as financial support from the DFG Grants No. AS120/10-1 and No. Ho 4489/4-1 (FOR 1807). We further thank J. Hofmann for helpful discussions.

APPENDIX A: EXACT RELATIONS TO THE CHARGE SPECTRUM

For the Holstein model, the phonon propagators (26) and (27) as well as the energies (29)–(31) are determined by the time-displaced charge correlation function $C_\rho(q,\tau-\tau') = \langle\rho_q(\tau)\rho_{-q}(\tau')\rangle$. The latter is related to the dynamic charge structure factor

$$S_\rho(q,\omega) = \frac{1}{Z}\sum_{mn} e^{-\beta(E_m-\mu N_m)}|\langle m|\hat{\rho}_q|n\rangle|^2 \times \delta(E_n - E_m - \omega) \tag{A1}$$

via $C_\rho(q,\tau) = \int_0^\infty d\omega\, K(\tau,\omega)\, S_\rho(q,\omega)$, where $K(\tau,\omega) = \exp[-\tau\omega] + \exp[-(\beta-\tau)\omega]$. Therefore, the entire single-particle dynamics of the phonons is contained in $S_\rho(q,\omega)$. In particular, $B(q,\omega)$ is directly related to $S_\rho(q,\omega)$ [45]. The energies (29)–(31) can be calculated from $S_\rho(\omega) = \sum_q S_\rho(q,\omega)$ via

$$E_{\rm ph}^{\rm kin} = \frac{E_{\rm ph}^0}{2} - 2\lambda t\int_0^\infty d\omega\, K_{--}(\omega/\omega_0,\beta\omega_0)\, S_\rho(\omega), \tag{A2}$$

$$E_{\rm ph}^{\rm pot} = \frac{E_{\rm ph}^0}{2} + 2\lambda t\int_0^\infty d\omega\, K_{++}(\omega/\omega_0,\beta\omega_0)\, S_\rho(\omega), \tag{A3}$$

$$E_{\rm eph} = -4\lambda t\int_0^\infty d\omega\, K_{+}(\omega/\omega_0,\beta\omega_0)\, S_\rho(\omega), \tag{A4}$$

with the kernels ($x = \omega/\omega_0$, $y = \beta\omega_0$, $\omega_0 > 0$)

$$K_{\pm\pm}(x,y) = \frac{1}{4\pi(x^2-1)}\left\{x\tanh(xy/2)\coth(y/2) \pm \frac{xy\tanh(xy/2)}{2\sinh^2(y/2)} \mp \frac{2x}{(x^2-1)}[\tanh(xy/2)\coth(y/2) - x^{\mp 1}]\right\}, \tag{A5}$$

and $K_+ = K_{++} + K_{--}$, with

$$K_+(x,y) = \frac{x\tanh(xy/2)\coth(y/2) - 1}{2\pi(x^2-1)}. \tag{A6}$$

The kernels are plotted in Fig. 4 for different temperatures. At $T = 0$, K_{++} and K_+ are largest at $\omega = 0$ and decrease monotonically with increasing ω, whereas K_{--} is zero at $\omega = 0$ and has a maximum at $\omega = \omega_0$. Therefore, $E_{\rm ph}^{\rm pot}$ and

E_{eph} mainly capture the charge ordering. In contrast, because K_{--} filters out the zero-frequency contributions to $S_\rho(\omega)$, $E_{\mathrm{ph}}^{\mathrm{kin}}$ reveals the softening of the phonons and the opening of the Peierls gap. The same reasoning applies to the phonon spectral function. If calculated from Eq. (26) it is dominated by the central mode in the Peierls phase. This mode is filtered out when using Eq. (27). The kernels broaden significantly when the temperature becomes comparable to ω_0 but the qualitative behavior for $\omega \ll \omega_0$ remains unchanged.

APPENDIX B: TRANSLATIONAL INVARIANCE OF THE VERTICES

The bosonic estimators from the distribution of vertices can be substantially improved by exploiting translational invariance in imaginary time: replacing $\tau_k \to \tau_k + \Delta\tau$ and $\tau_k' \to \tau_k' + \Delta\tau$ for all vertices $k \in \{1, \ldots, n\}$ leaves the weight $W[C_n]$ unchanged. Thereby, we can derive improved estimators for the bosonic energies (35) and (36) as well as the phonon propagator (43).

For the energies (35) and (36), translational invariance allows for the transformation

$$\frac{P_\pm(\tau_k)P_\pm(\tau_k')}{P_+(\tau_k-\tau_k')} \longrightarrow \underbrace{\frac{1}{\beta}\int_0^\beta d\tau\, \frac{P_\pm(\tau_k+\tau)P_\pm(\tau_k'+\tau)}{P_+(\tau_k-\tau_k')}}_{\bar{P}_\pm(\tau_k-\tau_k')} \tag{B1}$$

to the averaged propagator ($\tau \in [-\beta,\beta]$)

$$\bar{P}_\pm(\tau) = \frac{1}{2\beta} \pm \frac{\omega_0}{4}\frac{\beta-|\tau|}{\beta}\left[\coth(\omega_0\beta/2) - \frac{P_-(\tau)}{P_+(\tau)}\right] \pm \frac{\omega_0}{4}\frac{|\tau|}{\beta}\left[\coth(\omega_0\beta/2) + \frac{P_-(\tau)}{P_+(\tau)}\right]. \tag{B2}$$

Since the substitution (B1) applies to time differences of the same vertex, the computational cost to calculate the energies remains $\mathcal{O}(n)$. The improvement is particularly noticeable for $E_{\mathrm{ph}}^{\mathrm{kin}}$ (see Sec. V A).

The simplest way to calculate the phonon propagators (42) and (43) is to fix the second time argument to $\tau' = 0$ and apply Eq. (9) to obtain the necessary information from the vertices in $\mathcal{O}(nN_\tau)$ operations. Similar to the equal-time case, especially the estimator for the momentum correlations can be improved by using translational invariance. However, the rigorous approach of integrating over all translations increases the computational cost to $\mathcal{O}(n^2N_\tau)$ operations since the sums in the first term of Eq. (9) can no longer be calculated independently. This problem can be overcome by measuring the correlation functions on an equidistant grid with spacing $\Delta\tau_{\mathrm{obs}}$ so that translations of all vertices by multiples of $\Delta\tau_{\mathrm{obs}}$ are available and the computational cost remains $\mathcal{O}(nN_\tau)$. Regardless, translational invariance can be applied rigorously to the second term in Eq. (9). Putting the contributions of the phonon propagator together requires another $\mathcal{O}(L^2N_\tau^2)$ operation, where an additional factor of N_τ comes from exploiting translational invariance. This last step dominates the computational time for vertex measurements (cf. Sec. V A).

[1] R. Blankenbecler, D. J. Scalapino, and R. L. Sugar, Phys. Rev. D **24**, 2278 (1981).
[2] A. W. Sandvik and J. Kurkijärvi, Phys. Rev. B **43**, 5950 (1991).
[3] A. N. Rubtsov, V. V. Savkin, and A. I. Lichtenstein, Phys. Rev. B **72**, 035122 (2005).
[4] P. Werner, A. Comanac, L. de' Medici, M. Troyer, and A. J. Millis, Phys. Rev. Lett. **97**, 076405 (2006).
[5] E. Gull, A. J. Millis, A. I. Lichtenstein, A. N. Rubtsov, M. Troyer, and P. Werner, Rev. Mod. Phys. **83**, 349 (2011).
[6] M. Iazzi and M. Troyer, Phys. Rev. B **91**, 241118 (2015).
[7] L. Wang, M. Iazzi, P. Corboz, and M. Troyer, Phys. Rev. B **91**, 235151 (2015).
[8] S. Chandrasekharan, Phys. Rev. D **82**, 025007 (2010).
[9] S. Chandrasekharan, Eur. Phys. J. A **49**, 1 (2013).
[10] Z.-X. Li, Y.-F. Jiang, and H. Yao, Phys. Rev. B **91**, 241117 (2015).
[11] L. Wang, Y.-H. Liu, M. Iazzi, M. Troyer, and G. Harcos, Phys. Rev. Lett. **115**, 250601 (2015).
[12] M. B. Hastings, I. González, A. B. Kallin, and R. G. Melko, Phys. Rev. Lett. **104**, 157201 (2010).
[13] S. Humeniuk and T. Roscilde, Phys. Rev. B **86**, 235116 (2012).
[14] T. Grover, Phys. Rev. Lett. **111**, 130402 (2013).
[15] F. F. Assaad, T. C. Lang, and F. Parisen Toldin, Phys. Rev. B **89**, 125121 (2014).
[16] F. F. Assaad, Phys. Rev. B **91**, 125146 (2015).
[17] P. Broecker and S. Trebst, J. Stat. Mech. (2014) P08015.
[18] L. Wang and M. Troyer, Phys. Rev. Lett. **113**, 110401 (2014).
[19] J. E. Drut and W. J. Porter, Phys. Rev. B **92**, 125126 (2015).
[20] W.-L. You, Y.-W. Li, and S.-J. Gu, Phys. Rev. E **76**, 022101 (2007).
[21] D. Schwandt, F. Alet, and S. Capponi, Phys. Rev. Lett. **103**, 170501 (2009).
[22] A. F. Albuquerque, F. Alet, C. Sire, and S. Capponi, Phys. Rev. B **81**, 064418 (2010).
[23] L. Wang, Y.-H. Liu, J. Imriška, P. N. Ma, and M. Troyer, Phys. Rev. X **5**, 031007 (2015).
[24] D. J. Luitz and F. F. Assaad, Phys. Rev. B **81**, 024509 (2010).
[25] F. F. Assaad and T. C. Lang, Phys. Rev. B **76**, 035116 (2007).
[26] M. Hohenadler, H. Fehske, and F. F. Assaad, Phys. Rev. B **83**, 115105 (2011).
[27] M. Hohenadler, F. F. Assaad, and H. Fehske, Phys. Rev. Lett. **109**, 116407 (2012).
[28] M. Hohenadler, Phys. Rev. B **88**, 064303 (2013).
[29] M. Weber, F. F. Assaad, and M. Hohenadler, Phys. Rev. B **91**, 245147 (2015).
[30] R. P. Feynman, Phys. Rev. **97**, 660 (1955).
[31] M. Hohenadler and T. C. Lang, in *Computational Many-Particle Physics*, edited by H. Fehske, R. Schneider, and A. Weiße (Springer, Berlin, 2008), pp. 357–366.
[32] T. Holstein, Ann. Phys. (NY) **8**, 325 (1959); **8**, 343 (1959).

[33] J. E. Hirsch, Phys. Rev. B **28**, 4059 (1983).
[34] P. Werner and A. J. Millis, Phys. Rev. Lett. **104**, 146401 (2010).
[35] H. Hafermann, Phys. Rev. B **89**, 235128 (2014).
[36] P. Werner and M. Casula, J. Phys.: Condens. Matter **28**, 383001 (2016).
[37] P. Sun and G. Kotliar, Phys. Rev. B **66**, 085120 (2002).
[38] T. Ayral, S. Biermann, and P. Werner, Phys. Rev. B **87**, 125149 (2013).
[39] J. E. Hirsch and E. Fradkin, Phys. Rev. Lett. **49**, 402 (1982).
[40] E. Jeckelmann, C. Zhang, and S. R. White, Phys. Rev. B **60**, 7950 (1999).
[41] N. Metropolis, A. W. Rosenbluth, M. N. Rosenbluth, A. H. Teller, and E. Teller, J. Chem. Phys. **21**, 1087 (1953).
[42] W. K. Hastings, Biometrika **57**, 97 (1970).
[43] A. W. Sandvik, R. R. P. Singh, and D. K. Campbell, Phys. Rev. B **56**, 14510 (1997).
[44] S.-J. Gu, Int. J. Mod. Phys. B **24**, 4377 (2010).
[45] M. Weber, F. F. Assaad, and M. Hohenadler, Phys. Rev. B **91**, 235150 (2015).
[46] J. Greitemann, S. Hesselmann, S. Wessel, F. F. Assaad, and M. Hohenadler, Phys. Rev. B **92**, 245132 (2015).
[47] J. E. Hirsch and E. Fradkin, Phys. Rev. B **27**, 4302 (1983).
[48] M. Hohenadler and F. F. Assaad, Phys. Rev. B **87**, 075149 (2013).
[49] H. Bakrim and C. Bourbonnais, Phys. Rev. B **91**, 085114 (2015).
[50] R. T. Clay and R. P. Hardikar, Phys. Rev. Lett. **95**, 096401 (2005).
[51] M. Hohenadler, G. Wellein, A. R. Bishop, A. Alvermann, and H. Fehske, Phys. Rev. B **73**, 245120 (2006).
[52] S. Ejima and H. Fehske, Europhys. Lett. **87**, 27001 (2009).
[53] H. Fehske, G. Hager, and E. Jeckelmann, Europhys. Lett. **84**, 57001 (2008).
[54] J. Ranninger and U. Thibblin, Phys. Rev. B **45**, 7730 (1992).
[55] M. Hohenadler, H. G. Evertz, and W. von der Linden, Phys. Rev. B **69**, 024301 (2004).
[56] E. C. Creffield, G. Sangiovanni, and M. Capone, Eur. Phys. J. B **44**, 175 (2005).
[57] S. Sykora, A. Hübsch, K. W. Becker, G. Wellein, and H. Fehske, Phys. Rev. B **71**, 045112 (2005).
[58] A. W. Sandvik, Phys. Rev. B **57**, 10287 (1998).
[59] K. S. D. Beach, arXiv:cond-mat/0403055.
[60] G. Sun, A. K. Kolezhuk, and T. Vekua, Phys. Rev. B **91**, 014418 (2015).
[61] Jülich Supercomputing Centre, J. Large-scale Res. Facil. **2**, A62 (2016).